Inorganic Chemistry

pubs.acs.org/IC

Article

Spin Reorientation in Antiferromagnetic $MnPd_5Se$ with an Anti-$CeCoIn_5$ Structure Type

Ranuri S. Dissanayaka Mudiyanselage, Qiang Zhang, Madalynn Marshall, Mark Croft, Zhixue Shu, Tai Kong, and Weiwei Xie*

Cite This: *Inorg. Chem.* 2022, 61, 3981−3988

Read Online

ACCESS | Metrics & More | Article Recommendations | Supporting Information

ABSTRACT: $MnPd_5Se$, a derivative of the anti-$CeCoIn_5$-type phase, was synthesized from a high-temperature solid-state reaction, structurally determined by X-ray diffraction, and magnetically characterized with a combined magnetic measurement and neutron powder diffraction (NPD). According to the X-ray diffraction results, $MnPd_5Se$ crystallizes in a layered tetragonal structure with the same space group as $CeCoIn_5$, $P4/mmm$ (No. 123). $MnPd_5Se$ shows antiferromagnetic ordering around 80 K on the basis of the magnetic property measurements. An A-type antiferromagnetic structure was revealed from the analysis of neutron powder diffraction results at 300, 50, and 6 K. Moreover, a spin orientation rotation was observed as the temperature decreased. Pd L_3 X-ray absorption near edge spectroscopy results for $MnPd_5Se$ semiqualitatively correlate with the calculated density of states supporting a nominal 0.2 electron transfer into the Pd d orbital from either Se or Mn in the compound. The discovery of $MnPd_5Se$, along with our previously reported MnT_5Pn (T = Pd or Pt; Pn = P or As), provides a tunable system for studying the magnetic ordering from ferromagnetism to antiferromagnetism with the strong spin−orbit coupling effect.

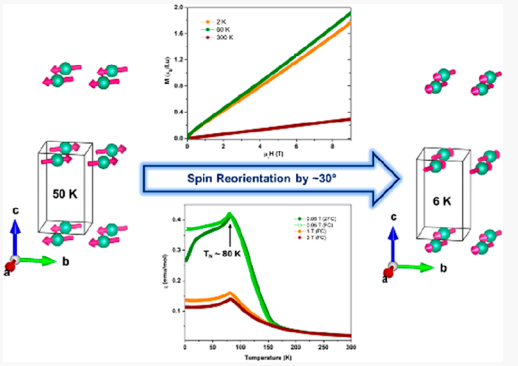

INTRODUCTION

Understanding, further design, and synthesis of rare-earth-free magnetic intermetallic materials with high transition temperatures and large magnetic moments are essential for applied information technology, such as magnetic and magnetoelastic devices, spintronics, and even biomedical sensors. In the past several decades, most research was focused on complex intermetallic compounds containing magnetically active Mn, Fe, and Co atoms.[1−4] By tuning various 3d transition metal interactions, one can determine and analyze the magnetic exchange as a function of atomic distances and chemical bonding interactions.[2,5−7] The previous research shows that the magnetic ordering that originated from magnetic interlayer exchange interaction is extremely sensitive to magnetically atomic distances.[7−9] Moreover, it has been reported that the transformation between ferromagnetic (FM) states and antiferromagnetic (AFM) states can be manipulated by various parameters, such as temperature, pressure, applied magnetic field, and defects, for example, topological magnetic RMn_6X_6 and RMn_2X_2 (R = rare-earth element; X = Sn or Ge).[9−12] On the contrary, heavy-Fermion system $CeCoIn_5$-type compounds with tetragonal lattice symmetry make up the family that has been well studied in terms of the transformation between superconductivity and magnetism.[13−17] Recently, a new family of compounds with anti-$CeCoIn_5$ structure was discovered with diverse physical properties, such as the rare-earth-free ferromagnetic $MnPt_5As$, Yb_xPt_5P with the coexistence of superconductivity and magnetism, spin-flop $FePt_5P$, etc.[18−20] The magnetically atomic distance between layers can be easily tuned by chemical doping. Furthermore, the spin−orbit coupling (SOC) effect can strongly influence the magnetic ordering. To further understand how valence electron counts and electronegativity govern the magnetic ordering, the Group V elements P and As were replaced with Se atoms. A new compound, $MnPd_5Se$, was synthesized accordingly. $MnPd_5Se$ with the same structure as MnT_5Pn (T = Pd or Pt; Pn = P or As) was determined to order antiferromagnetically with a T_N of ∼80 K. The neutron scattering experiments show the magnetic moment vector rotation as the temperature decreases. The new antiferromagnetic $MnPd_5Se$, along with our previously reported MnT_5Pn (T = Pd or Pt; Pn = P or As), can be an ideal platform for investigating the tunable magnetism in rare-earth-free magnetic intermetallics.

EXPERIMENTAL SECTION

Synthesis. Polycrystalline $MnPd_5Se$ was synthesized by the solid-state high-temperature pellet method. Mn powder (Mangan, >99%),

Received: November 21, 2021
Published: February 22, 2022

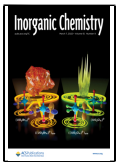

Pd powder (BTC, −200 mesh, 99.95%), and Se shots (BTC, 99.999%) were weighed in a 1:5:1 Mn:Pd:Se atomic ratio. The mixture was ground well and pressed into a pellet with a total mass of 200 mg. The pellet was placed in an alumina crucible and sealed into an evacuated silica ampule ($<10^{-5}$ Torr). The sample tube was heated to 1050 °C at a rate of 40 °C/h, annealed at 1050 °C for 48 h before, and then slowly cooled to room temperature at a rate of 10 °C/h. The reaction scheme yielded small single-crystal $MnPd_5Se$, which was stable in air and moisture.

Phase Identification and Structural Analysis of $MnPd_5Se$. The crystal structure of $MnPd_5Se$ was determined by a Bruker D8 EcoQuest Single Crystal X-ray Diffractometer (SC-XRD) with Mo radiation ($\lambda_{K\alpha}$ = 0.71073 Å). Multiple single crystals were tested to confirm the purity, and the crystal structure was determined using the SHELXTL package with direct methods and full-matrix least squares on the F^2 model.[21,22] Atomic mixtures and vacancies were tested in the refinement. The powder X-ray diffraction (PXRD) pattern was collected using the Bruker D2 Phaser XE-T edition benchtop X-ray powder diffractometer with Cu radiation ($\lambda_{K\alpha}$ = 1.5405 Å) over a range of Bragg angles (2θ) from 5° to 90°. LeBail fitting of PXRD data was conducted in the Fullprof Suite software.[23]

Scanning Electron Microscope (SEM). To further evaluate the chemical composition, the sample was analyzed using a high-vacuum Zeiss Sigma field emission SEM (FESEM) with an Oxford INCA PentaFETx3 Energy-Dispersive Spectroscopy (EDS) system. Spectra were recorded from multiple areas of the crystals mounted on a carbon tape with an accelerating voltage of 30 keV.

X-ray Absorption Near Edge Spectroscopy (XANES). Pd-L3 XANES data were collected in total electron yield mode, with sequential standards for calibration, on the Brookhaven National Synchrotron Light Source II (NSLS-II) insertion device beamline 7-ID-2 SST-2 using a Si-111 monochromator. Here the total electron yield mode was important for minimizing self-absorption rounding of the spectra.

Neutron Powder Diffraction (NPD). To determine the magnetic structure of the titled compound, neutron powder diffraction patterns were collected on the time-of-flight (TOF) powder diffractometer (POWGEN) at the Spallation Neutron Source (SNS) at Oak Ridge National Laboratory (ORNL). Multiple reactions were carried out as explained in the previous section to synthesize high-quality single crystals for the NPD experiments, and the purity of the products from each reaction was confirmed with PXRD. A powder sample of ∼1.6 g was loaded into a 6 mm diameter vanadium sample can with a copper gasket inside the argon gas-filled glovebox. The data were collected at temperatures of 6, 50, and 300 K using a neutron wavelength band (2.13−3.198 Å) with a center wavelength of 2.665 Å. The nuclear structure was determined from the data collected at 300 K using the FullProf refinement suite, while magnetic structure analysis at low temperatures was performed using the FullProf refinement suite and the SARAh Representational Analysis and Refine Software.[23−25] The *k*-search functionality within FullProf revealed a commensurate magnetic propagation vector of $\mathbf{k} = (0, 0, {}^1/_2)$ for $MnPd_5Se$. The representational analysis of the propagation vector in the parent *P*4/*mmm* space group was performed using SARAh and resulted in three unique irreducible representations with basis vectors, similar to the reported $MnPt_5P$ magnetic structure analysis.[26]

Physical Property Measurements. Magnetic properties and heat capacity measurements were conducted on a Quantum Design Dynacool physical property measurement system (PPMS). The instrument operates from 1.8 to 300 K with applied fields of ≤9 T. The magnetic susceptibility is defined as $\chi = M/H$, where M is the magnetization in units of electromagnetic unit and H is the external magnetic field. The standard relaxation calorimetry method was used to measure the heat capacity. Data were collected from 1.8 to 150 K using N-type grease.

RESULTS AND DISCUSSION

Structural Analysis of $MnPd_5Se$. $MnPd_5Se$, which is the first ternary compound of the Mn−Pd−Se system, crystallizes in a $TlPd_5As$-type structure in space group *P*4/*mmm* (No. 123). The refined crystallographic data, atomic coordination information, and anisotropic displacement parameters are listed in Tables 1 and 2. The only difference between the $CeCoIn_5$-type structure and $MnPd_5Se$ is the interchange of Pd on the 1*a* site and the Mn atom on the 1*c* site. When $MnPd_5Se$ was modeled with the $CeCoIn_5$-type structure, the residual values increased, excluding the existence of this alternative $CeCoIn_5$-type structure in $MnPd_5Se$. Furthermore, the partial and mixed occupancy was tested, and the results led to the conclusion that neither is observed for $MnPd_5Se$. As shown in panels a and b of Figure 1, $MnPd_5Se$ possesses a layered structure with Mn@Pd_{12} polyhedral layers intercalated between two-dimensional Se layers. The nearest neighbor Mn−Mn distance in the $a-b$ plane is ∼3.978 Å, whereas the interlayer Mn−Mn distance along the *c*-axis is ∼6.976 Å. The Pd1 atom at the origin is coordinated with four Mn atoms and the eight Pd2 atoms in a distorted cuboctahedron as shown in Figure 1b (bottom). Similarly, the Mn atom is in the center of a cuboctahedron surrounded by Pd atoms Figure 1b (top).

Table 1. Single-Crystal Refinement Data for $MnPd_5Se$ at 273(2) K

empirical formula	$MnPd_5Se$
formula weight (g/mol)	665.90
space group, Z	*P*4/*mmm*, 1
a (Å)	3.978(2)
c (Å)	6.976(5)
volume (Å^3)	110.4(1)
extinction coefficient	none
θ range (deg)	2.920−33.866
no. of reflections, R_{int}	670, 0.0358
no. of independent reflections	165
no. of parameters	13
R_1, ωR_2 [$I > 2\delta(I)$]	0.0390, 0.0933
R indices (all data) (R_1, ωR_2)	0.0538, 0.1010
goodness of fit on F^2	1.083
diffraction peak and hole (e$^-$/Å^3)	3.087 and −2.240

Table 2. Atomic Coordinates and Equivalent Isotropic Displacement Parameters of $MnPd_5Se$[a]

atom	Wyckoff	x	y	z	occupancy	U_{eq}
Mn	1*c*	${}^1/_2$	${}^1/_2$	0	1	0.0073(9)
Se	1*b*	0	0	${}^1/_2$	1	0.0060(7)
Pd1	1*a*	0	0	0	1	0.0062(6)
Pd2	4*i*	0	${}^1/_2$	0.2783(2)	1	0.0072(4)

[a] U_{eq} is defined as one-third of the trace of the orthogonalized $\mathbf{U}_{ij}$ tensor (square angstroms).

Phase and Chemical Composition Analysis. A Rietveld fitting of the PXRD pattern represented in Figure 1c indicates the purity of the bulk material is in agreement with the refined lattice parameters obtained from SC-XRD. The refinement results for R_p, R_{wp}, and χ^2 are 7.92, 10.7, and 2.22, respectively, which indicate a reasonable PXRD refinement. Furthermore, the Rietveld refinement of the nuclear neutron powder diffraction data at 300 K also confirms the purity of the bulk sample. The results of the refinement are given in Figure S1. In addition, the chemical compositions of the new material were further examined by SEM-EDS and found to have an average composition of $Mn_{1.0(1)}Pd_{5.08(5)}Se_{0.95(5)}$, which is in agreement

https://doi.org/10.1021/acs.inorgchem.1c03637
Inorg. Chem. 2022, 61, 3981−3988

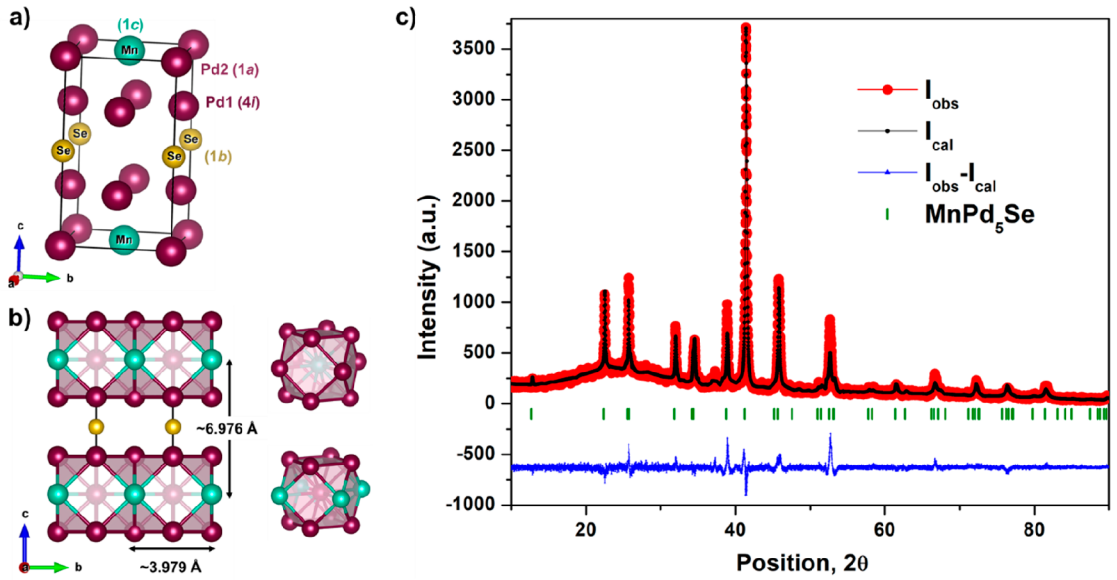

Figure 1. (a) Unit cell of $MnPd_5Se$. (b) Layered crystal structure of $MnPd_5Se$ with cuboctahedra showing Mn and Pd coordination. (c) Rietveld refinement of PXRD of $MnPd_5Se$.

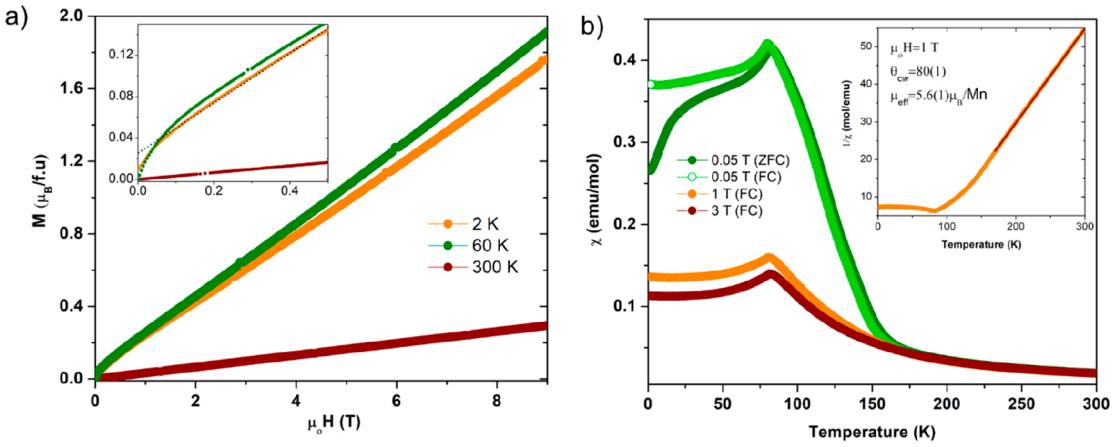

Figure 2. (a) Magnetization vs applied field up to 9 T at temperatures ranging from 2 to 300 K. The inset shows an enlarged view of low-field magnetization showing the extrapolation of the magnetization at 2 K as a dotted line. (b)*b*. Magnetic susceptibility vs temperature measured under fields of 0.05, 1, and 3 T. The inset shows the Curie−Wiess fitting of the inverse magnetic susceptibility at 1 T. FC and ZFC refer to field-cooled and zero-field-cooled methods, respectively.

with the SCXRD results. Detailed images and the composition of the multiple crystals examined via SEM-EDS are given in Table S1.

Antiferromagnetic Ordering Dominating in $MnPd_5Se$. Figure 2a illustrates the isothermal magnetization curves measured over the temperature range of 2−300 K with an applied field of ≤9 T on the polycrystalline $MnPd_5Se$ sample. The magnetization curve at 2 K increases sharply from 0 to ∼0.05 μ_B up to 500 Oe followed by a linear increment up to ∼2 μ_B, which appears to be unsaturated up to 9 T. This linear behavior of magnetization indicates a tendency toward an antiferromagnetic (AFM) interaction between the Mn atoms. However, as the temperature increases to 60 K, the magnetic moment is larger than that detected at 2 K. The unusual magnetic behaviors indicate more complicated magnetic ordering in the system. The extrapolation of the magnetization data at 2 K to zero applied field (shown as the dotted line in the inset of Figure 2a) gives a positive intercept of 0.025 μ_B to the magnetization axis. This residual moment was initially thought to be a weak ferromagnetism or spin canting, but what was observed was a spin reorientation according to neutron powder diffraction data analysis. Possible magnetic impurities such as $MnSe_2$ (ferromagnetic),[27] Mn_3Pd_5 (ferrimagnetic),[28] $MnPd_3$ (antiferromagnetic),[29] and other ferromagnetic Mn−Pd alloys with various Mn concentrations were tested with the PXRD refinement using FullProf Suite.[30] This magnetic behavior in the field-dependent magnetization may be attributed to a competing antiferromagnetic state with an intrinsic weak ferromagnetic transition. This has been further investigated using our neutron powder diffraction results.

The temperature dependence of the magnetic susceptibility (χ) measured under various fields for $MnPd_5Se$ is depicted in Figure 2b. When the temperature is decreased under an applied field of 0.05 T, the magnetic susceptibility increases rapidly around 150 K, reaching a maximum at ∼80 K, and then decreases upon further cooling. This steep increase in χ at 0.05 T around 150 K is characteristic of a ferromagnetic transition,

https://doi.org/10.1021/acs.inorgchem.1c03637
Inorg. Chem. 2022, 61, 3981−3988

while the peak at ∼80 K could originate from an antiferromagnetic state. However, when the applied field is increased, the weak ferromagnetic interactions observed at 0.05 T are suppressed while the antiferromagnetic behavior dominates, consistent with the isothermal magnetization data. Furthermore, Figure 2b illustrates a splitting of the zero-field cooling (ZFC) and field cooling (FC) curves at 0.05 T indicating magneto crystalline anisotropy or a coexistence of ferromagnetic and antiferromagnetic interactions or a spin canted state.[31−33] The magnetic susceptibility above 150 K (1 T) was used to fit the data with the Curie−Weiss law, $\chi = \chi_0 + \frac{C}{T-\theta_{CW}}$, where χ, χ_0, C, and θ_{CW} represent the magnetic susceptibility, the temperature-independent contribution to the susceptibility, the Curie constant, and the Curie−Weiss temperature, respectively. The Curie−Weiss fit yielded an effective moment of 5.6(1) μ_B/Mn and a positive θ_{CW} of 80(1) K. The positive θ_{CW} is not in agreement with the dominant antiferromagnetic behavior suggested by the magnetization results, thus indicating potential competing magnetic interactions.[34] Therefore, to investigate the magnetic structure of the new compound, neutron powder diffraction experiments were carried out.

On the contrary, to confirm the intrinsic magnetic ordering, heat capacity measurements were performed on the same piece of $MnPd_5Se$ that was used in the magnetic measurements. The results for heat capacity without an applied field are shown in Figure 3. The sharp peak observed around 80 K with a ΔC_p of

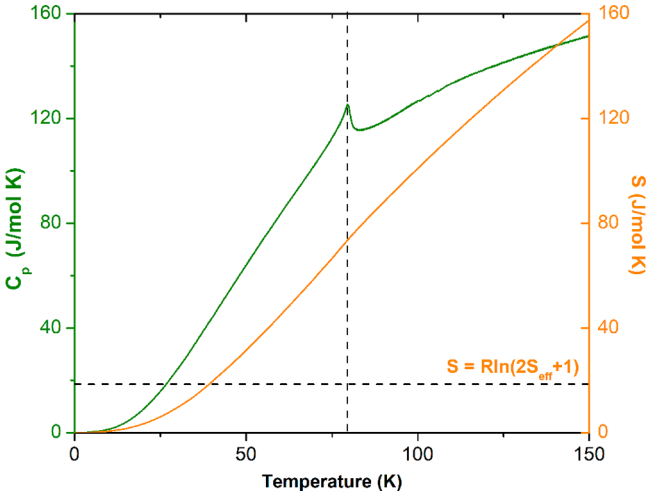

Figure 3. Heat capacity (C_p) measurements on $MnPd_5Se$ from 2 to 150 K on the left axis and change in entropy of the material with temperature on the right axis.

∼12 J mol^{-1} K^{-1} is attributed to the antiferromagnetic ordering of $MnPd_5Se$, which is consistent with the magnetization measurements. The entropy calculated from the integrated C_p/T data is shown on the right axis of Figure 3. According to the neutron powder diffraction analysis presented below, Mn in $MnPd_5Se$ ordered with an S_{eff} of 4.1(8) μ_B. Thus, the theoretical entropy change is expected to be $R\ln(2S_{eff} + 1)$ ∼ 18.5 J mol^{-1} K, which is marked in Figure 3.[35] However, due to the lack of information about the contributions of phonons to heat capacity, the experimental magnetic entropy of $MnPd_5Se$ could not be derived from heat capacity data.

Magnetic Structure of $MnPd_5Se$. To determine the magnetic structure of $MnPd_5Se$, the neutron powder diffraction (NPD) data were collected at 6, 50, and 300 K. The refined NPD patterns at 6, 50, and 300 K are given in Figure 4 and the Supporting Information. The analysis of NPD data at 300 K confirms the tetragonal $P4/mmm$ structure of $MnPd_5Se$ and the purity of the bulk sample, which agrees with the SCXRD and PXRD results. Upon cooling to 50 K, a set of magnetic peaks were detected and reasonably indexed by the propagation vector $\mathbf{k} = (0, 0, {}^1/_2)$, indicating that the magnetic unit cell $a \times b \times 2c$ is double the crystal unit cell along the c-axis for the $MnPd_5Se$ phase. The magnetic moments continue to order down to 6 K as shown by the increase in the magnetic moment from 3.1(6) to 4.1(8) μ_B/Mn from 50 to 6 K, respectively. Furthermore, the refinement reveals that the magnetic moments are confined in the $a-b$ plane at both 6 and 50 K. The calculated ordered magnetic moment at 50 K has the components μ_a = 1.8(5) μ_B/Mn and μ_b = −2.5(4) μ_B/Mn with a total magnetic moment of μ_{tot} = 3.1(6) μ_B/Mn, whereas upon cooling to 6 K, the components of μ_a = 3.6(4) μ_B/Mn and μ_b = −1.9(8) μ_B/Mn with a total ordered moment of 4.1(8) μ_B/Mn were determined. Detailed values of the moments along the different crystal axes are listed in Table 3. Figure 5 represents the magnetic structure of $MnPd_5Se$ at 50 and 6 K. The magnetic moments obtained from neutron diffraction are smaller than the saturated moments measured at 1.8 K, which may result from the measured temperature differences. The results reveal that the compound has an A-type antiferromagnetic structure where the spins align ferromagnetically within the $a-b$ plane and align antiferromagnetically between the Mn layers along the c-axis. These results are in agreement with the positive θ_{CW} value corresponding to the ferromagnetic interactions in the $a-b$ plane, while the sharp peak observed in magnetic susceptibility measurements, which is characteristic of an antiferromagnetic transition, is consistent with the interlayer antiferromagnetic ordering. Furthermore, cooling to 6 K resulted in a rotated AFM axis as shown in the schematic diagram in Figure 5c. The rotation angle was calculated considering the ordered magnetic moments along directions a and b and found to deflect 27.2° toward the a-axis. Thus, the residual magnetization observed at 2 K in the isothermal magnetization curve could originate from this spin rotation state. Spin reorientation has been observed in a variety of Mn compounds such as MnBi, CeMnAsO, Pr-doped $Yb_{14}MnSb_{11}$, and $REMnO_3$.[36−39] These studies show that the crystalline electric field (CEF) and the subsequent large anisotropy play a key role in the spin reorientation of these materials. However, even though the parent $Yb_{14}MnSb_{11}$ compound shows anisotropy, spin reorientation is induced only when the doped Pr changes the 3d−3d interaction between $[MnSb_4]^{9-}$ layers via 3d−4f interactions.[36,40] Moreover, the anisotropic thermal expansion observed in MnBi that largely originated from nominally nonmagnetic Bi atoms with SOC strongly influences the spin reorientation behavior.[37] Thus, the temperature-dependent spin reorientation observed in $MnPd_5Se$ may originate from altered Mn 3d−3d interactions through 3d−4d (Mn−Pd) interaction with SOC. Furthermore, two kinds of spin reorientation have been previously reported: (1) sharp spin reorientation with a first-order phase transition and (2) a gradual tilt of spins with a second-order phase transition.[36,41−43] Accordingly, the spin reorientation observed in $MnPd_5Se$ can be attributed to a slow tilt of spins, which is also supported by the broad peak observed from heat capacity measurement at low temperatures.

https://doi.org/10.1021/acs.inorgchem.1c03637
Inorg. Chem. 2022, 61, 3981−3988

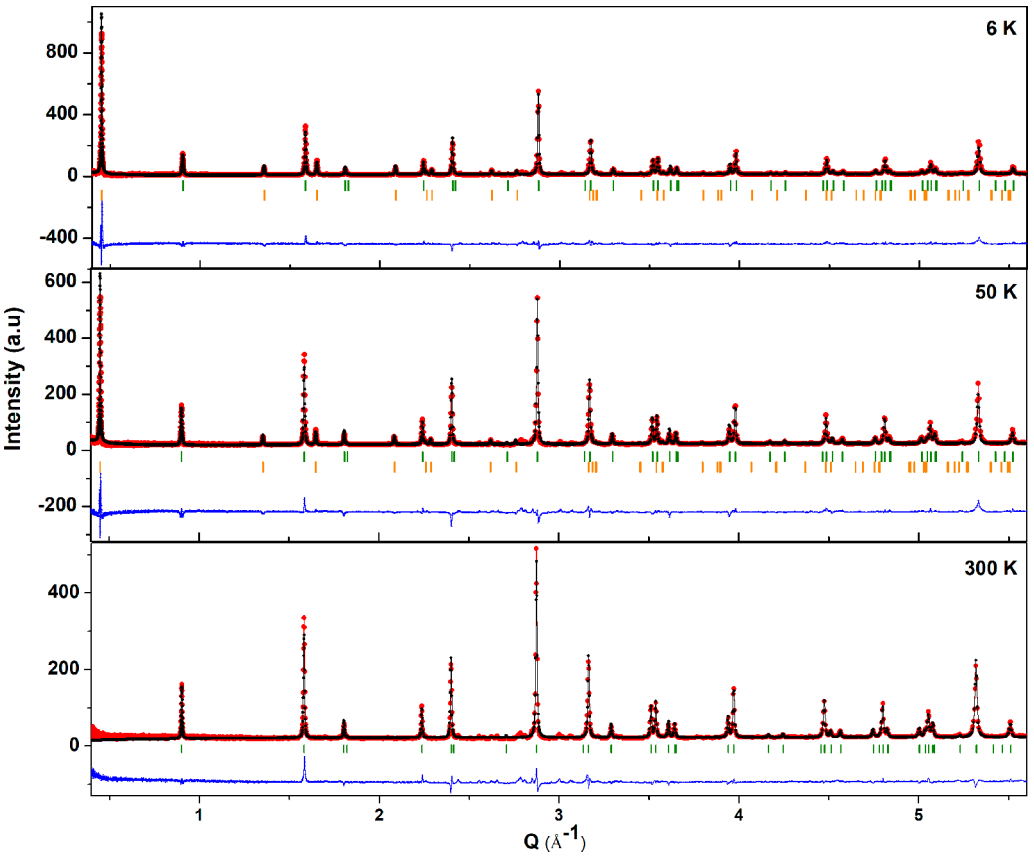

Figure 4. Refined neutron powder diffraction patterns at 300, 50, and 6 K.

Table 3. Projection on Each Crystal Axis from Magnetic Moments on Mn in $MnPd_5Se$

		magnetic moment (μ_B)	
translation	crystal axis	6 K	50 K
(0, 0, 0)	*a*	3.6(4)	1.8(5)
	b	−1.9(8)	−2.5(4)
	c	0.000	0.000
(0, 0, 1)	*a*	−3.6(4)	−1.8(5)
	b	1.9(8)	2.5(4)
	c	0	0
total		4.1(8)	3.1(6)

Pd Configuration and Electronic Structure of $MnPd_5Se$. The $L_{2,3}$ edges of the 5d/4d row of transition metal (T) materials manifest sharp "white line" (WL) features due to transitions into empty d states above the Fermi level (E_F).[44−50] The differing details of the $d_{5/2}$ and $d_{3/2}$ contributions to the WL features at the $L_{2,3}$ edges are beyond the scope of this paper on zeroth-order charge transfer and bonding effects. Evidence that the intensity and energy distribution of the WL feature reflect the d hole state count/distribution, weighted by matrix elements, has been indicated in elemental,[44,46,50] alloy,[48,49] and intermetallic[44−47] materials. In Figure 6a (bottom), the L_3 edge absorption coefficient (μ) spectrum of elemental ~d^9 Pd displays a sharp/intense WL feature due to transitions into the 4d hole state impinging on E_F. In contrast, the ~d^{10} Ag spectrum shows no WL but only a structured onset of transitions into the itinerant continuum states above E_F. (Here the Ag spectrum has been greatly shifted in energy for comparison.) Turning to the $MnPd_5Se$, Pd L_3 spectrum in Figure 6a (bottom), we find the WL feature is still quite sharp; however, its intensity is dramatically decreased relative to that of elemental Pd. This would support electron transfer into the 4d orbitals shifting them below E_F in this compound. To illustrate the WL feature only spectral contributions, a shifted Ag spectrum has been subtracted from the Pd spectra and the resulting absorption coefficient difference spectra ($\Delta\mu$) are displayed in Figure 6a (top). The energy shift of the subtracted Ag spectrum has been chosen so that the first shoulder of the subtracted spectrum lies under the center of each of the WL feature peaks. In Figure 6a (top), the WL feature of elemental Pd can be seen to be asymmetric with a sharper spectral cutoff on the low-energy (E_F) side. The very notably lower-intensity $MnPd_5Se$ WL feature is weekly broadened with a modest intensity enhancement on the high-energy side. The integrated $MnPd_5Se$ WL feature intensity is 20% less than that of elemental Pd, supporting a nominal 0.2 electron transfer into the Pd d orbital in the compound from either Se or Mn.[44−50] The broadening of the WL feature on the high-energy side suggests the upshifting of the energy of some antibonding 4d states in the compound.[45,46,48−50] Figure 6b presents the Pd d-projected DOS on the same energy scale as the XANES results for $MnPd_5Se$.[45,46,48−50] Here the compound Pd-DOS is dominated by the 4-fold more numerous Pd2 sites. The higher-energy broadening of both the WL feature and the Pd-DOS in the ~3 eV above the aligned peaks provides a semiqualitative correlation between the two despite the much lower energy resolution of the XANES.

The density of states (DOS) from −2 to 2 eV calculated from the *wien2k* package for $MnPd_5Se$ is shown in Figure 7.

https://doi.org/10.1021/acs.inorgchem.1c03637
Inorg. Chem. 2022, 61, 3981−3988

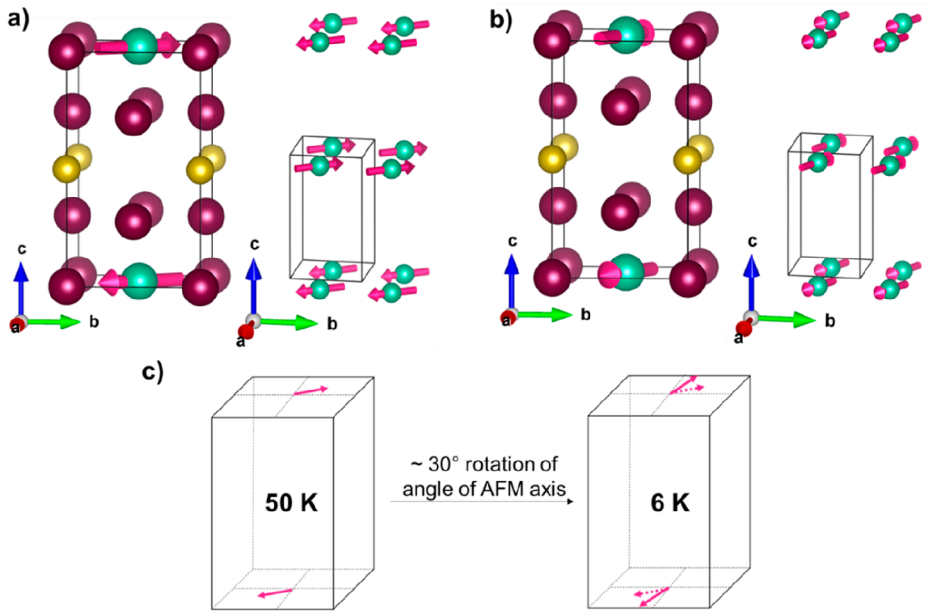

Figure 5. Magnetic structure of $MnPd_5Se$ refined from NPD at (a) 50 K and (b) 6 K showing the interlayer and intralayer magnetic interactions at 50 and 6 K. (c) Schematic representation of the AFM axis rotation with cooling.

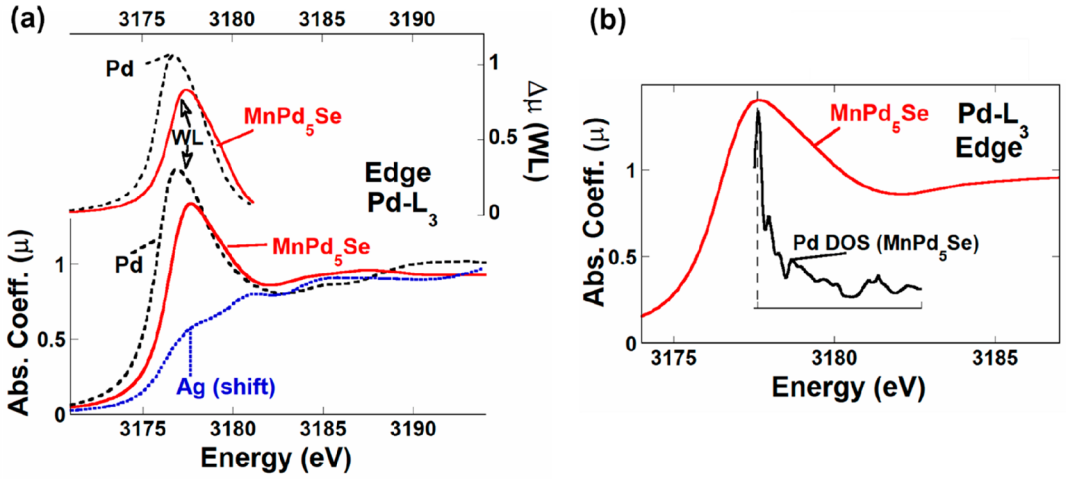

Figure 6. (a) Pd L_3 edges, with the WL features indicated, for $MnPd_5Se$ and elemental Pd (bottom). For comparison, the energy-shifted elemental Ag L_3 edge, with a negligible WL feature, is shown. Approximation of the WL features for the Pd spectra obtained by subtracting the Ag L_3 spectrum with an energy shift placing it at the center of the WL feature for each material (top). (b) Pd L_3 edge spectrum of $MnPd_5Se$ compared to the superimposed calculated DOS above E_F for Pd states in $MnPd_5Se$. Here the dashed vertical line indicates the E_F in the calculation.

The DOS for the energy range from −6 to 8 eV is presented in Figure S2. The DOS was determined first without applying SOC and spin polarization (SP) using the experimentally crystallographic unit cell information. The results indicate that there is a large density of states near the Fermi level where the major contribution is coming from Mn d orbitals and then from both Pd d atoms while the Se p orbital has the smallest contribution. Next, the SOC and SP effects were considered in the calculation, and here the magnetic unit cell determined from NDP analysis was utilized. The doubled unit cell used in this case is shown in Figure S3. As indicated in Figure 7b, the DOS at E_F for $MnPd_5Se$ has decreased significantly when both SOC and SP have been included. In $MnPd_5Se$, due to antiferromagnetic ordering, the Mn orbital contribution near E_F has been minimized by concentrating the major Mn1 and Mn2 orbital contributions around 1.5 and −1 eV, respectively. Additionally, Mn1, Mn2, Se, Pd1, and Pd2 hybridize near E_F, decreasing the corresponding DOS, while Pd3 and Pd4 in the 4*i* site contribute most to the Van Hove singularity near E_F. Furthermore, the electronic structure of $MnPd_5Se$ displays a pseudogap at ∼0.3 eV.

CONCLUSION

In this paper, we discovered the first ternary compound in the Mn−Pd−Se system, antiferromagnetic $MnPd_5Se$. The crystal structure and magnetic properties were fully characterized by both X-ray diffraction and neutron scattering techniques. $MnPd_5Se$ crystallizes in the anti-$CeCoIn_5$ structure with a layered tetragonal structure (space group $P4/mmm$). Below T_N ∼ 80 K, the A-type antiferromagnetic ordering was detected along direction *c*. Temperature-dependent neutron scattering confirms a slow spin reorientation as the temperature decreases. Semiqualitative comparison of Pd-L_3 XANES results

https://doi.org/10.1021/acs.inorgchem.1c03637
Inorg. Chem. 2022, 61, 3981−3988

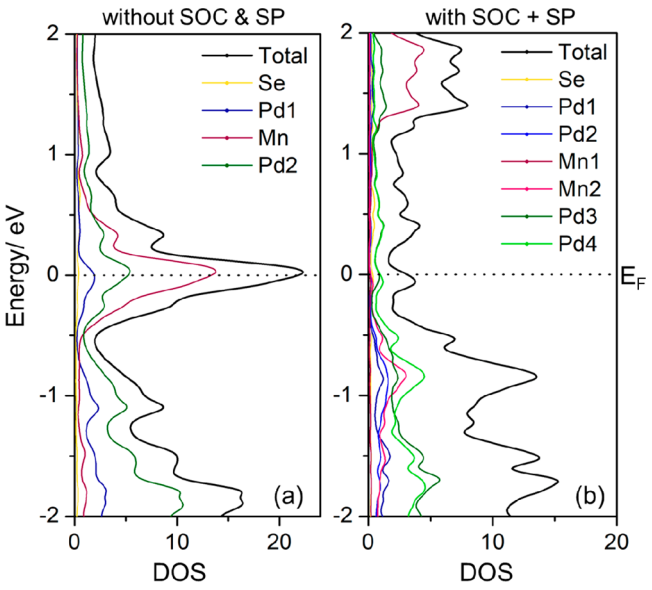

Figure 7. DOS of $MnPd_5Se$ calculated (a) without and (b) with SOC and SP.

and the DOS of the compound support the idea that the energies of some antibonding 4d states are increased with nominal 0.2 electron transfer into the Pd d orbital from either Mn or Se. Further manipulation of the spin reorientation intrinsic to $MnPd_5Se$ by doping with strong spin−orbit coupling elements could be interesting in future studies.

■ ASSOCIATED CONTENT

Supporting Information

The Supporting Information is available free of charge at https://pubs.acs.org/doi/10.1021/acs.inorgchem.1c03637.

SEM/EDS results of $MnPd_5Se$, nuclear structure refinement of $MnPd_5Se$ at 300 K, calculated DOS for $MnPd_5Se$, and magnetic unit cell of $MnPd_5Se$ (PDF)

Accession Codes

CCDC 2123586 contains the supplementary crystallographic data for this paper. These data can be obtained free of charge via www.ccdc.cam.ac.uk/data_request/cif, or by emailing data_request@ccdc.cam.ac.uk, or by contacting The Cambridge Crystallographic Data Centre, 12 Union Road, Cambridge CB2 1EZ, UK; fax: +44 1223 336033.

■ AUTHOR INFORMATION

Corresponding Author

Weiwei Xie − *Department of Chemistry and Chemical Biology, Rutgers University-New Brunswick, Piscataway, New Jersey 08854, United States;* orcid.org/0000-0002-5500-8195; Email: weiwei.xie@rutgers.edu

Authors

Ranuri S. Dissanayaka Mudiyanselage − *Department of Chemistry and Chemical Biology, Rutgers University-New Brunswick, Piscataway, New Jersey 08854, United States*

Qiang Zhang − *National Scattering Division, Oak Ridge National Laboratory, Oak Ridge, Tennessee 37831, United States;* orcid.org/0000-0003-0389-7039

Madalynn Marshall − *Department of Chemistry and Chemical Biology, Rutgers University-New Brunswick, Piscataway, New Jersey 08854, United States*

Mark Croft − *Department of Physics and Astronomy, Rutgers University-New Brunswick, Piscataway, New Jersey 08854, United States*

Zhixue Shu − *Department of Physics, University of Arizona, Tucson, Arizona 85721, United States*

Tai Kong − *Department of Physics, University of Arizona, Tucson, Arizona 85721, United States*

Complete contact information is available at: https://pubs.acs.org/10.1021/acs.inorgchem.1c03637

Notes

The authors declare no competing financial interest.

■ ACKNOWLEDGMENTS

The work at Rutgers is supported by National Science Foundation Grant DMR-2053287. Neutron diffraction measurements used resources at the Spallation Neutron Source, a U.S. Department of Energy Office of Science User Facility operated by the Oak Ridge National Laboratory. XANES was performed by Conan Weiland (NIST) on NSLS-II beamline 7-ID-2 SST-2 and supported in part under DOE-BES (DE-SC0012704).

■ REFERENCES

(1) Zhang, Y.; Miller, G. J.; Fokwa, B. P. T. Computational Design of Rare-Earth-Free Magnets with the $Ti_3Co_5B_2$-Type Structure. *Chem. Mater.* **2017**, *29* (6), 2535−2541.

(2) Shankhari, P.; Zhang, Y.; Stekovic, D.; Itkis, M. E.; Fokwa, B. P. T. Unexpected Competition between Antiferromagnetic and Ferromagnetic States in $Hf_2MnRu_5B_2$: Predicted and Realized. *Inorg. Chem.* **2017**, *56* (21), 12674−12677.

(3) Ko, H.; Gourdon, O.; Gout, D.; Mun, E.-D.; Thimmaiah, S.; Miller, G. J. Rhombohedrally Distorted γ-Brasses $Cr_{1-x}Fe_xGa$. *Inorg. Chem.* **2010**, *49* (24), 11505−11515.

(4) Thompson, C. M.; Kovnir, K.; Zhou, H.; Shatruk, M. Magnetism of Rare-Earth Cobalt Phosphides $GdCo_3P_2$ and $GdCo_5P_3$. *Z. Anorg. Allg. Chem.* **2011**, *637* (13), 2013.

(5) Canfield, P. C. Fishing the Fermi Sea. *Nature Phys.* **2008**, *4* (3), 167−169.

(6) Shankhari, P.; Scheifers, J. P.; Hermus, M.; Yubuta, K.; Fokwa, B. P. T. Unexpected Trend Deviation in Isoelectronic Transition Metal Borides $A_3T_5B_2$ (A = Group 4, T = Group 9): $Ti_3Co_5B_2$- vs. Perovskite-Type Studied by Experiments and DFT Calculations. *Zeitschrift für anorganische und allgemeine Chemie* **2017**, *643* (21), 1551−1556.

(7) Jia, S.; Jiramongkolchai, P.; Suchomel, M. R.; Toby, B. H.; Checkelsky, J. G.; Ong, N. P.; Cava, R. J. Ferromagnetic Quantum Critical Point Induced by Dimer-Breaking in $SrCo_2(Ge_{1-x}P_x)_2$. *Nature Phys.* **2011**, *7* (3), 207−210.

(8) Li, S.; Ao, Z.; Zhu, J.; Ren, J.; Yi, J.; Wang, G.; Liu, W. Strain Controlled Ferromagnetic-Antiferromagnetic Transformation in Mn-Doped Silicene for Information Transformation Devices. *J. Phys. Chem. Lett.* **2017**, *8* (7), 1484−1488.

(9) Brabers, J. H. V. J.; Buschow, K. H. J.; de Boer, F. R. Field-Induced First-Order Antiferromagnetic-Ferromagnetic Transitions in RMn_2Ge_2 Compounds and Their Relation to the Magnetostriction of the Mn Sublattice. *Phys. Rev. B* **1999**, *59* (14), 9314−9323.

(10) Xu, C. Q.; Heitmann, T. W.; Zhang, H.; Xu, X.; Ke, X. Magnetic Phase Transition, Magnetoresistance, and Anomalous Hall Effect in Ga-Substituted YMn_6Sn_6 with a Ferromagnetic Kagome Lattice. *Phys. Rev. B* **2021**, *104* (2), 024413.

(11) Eichenberger, L.; Haraux, P.; Venturini, G.; Malaman, B.; Mazet, T. Structural and Magnetic Properties of the New $Yb_{1-X}Sc_xMn_6Sn_6$ Solid Solution. *J. Alloys Compd.* **2019**, *775*, 883−888.

(12) Zhang, S.; Zhao, P.; Cheng, Z.; Li, R.; Sun, J.; Zhang, H.; Shen, B. Magnetism and Giant Magnetoresistance of $YMn_6Sn_{6-x}Ga_x$ (X = 0−1.8) Compounds. *Phys. Rev. B* **2001**, *64* (21), 212404.
(13) Blackburn, E.; Das, P.; Eskildsen, M. R.; Forgan, E. M.; Laver, M.; Niedermayer, C.; Petrovic, C.; White, J. S. Exploring the Fragile Antiferromagnetic Superconducting Phase in $CeCoIn_5$. *Phys. Rev. Lett.* **2010**, *105* (18), 187001.
(14) Hu, T.; Xiao, H.; Sayles, T. A.; Dzero, M.; Maple, M. B.; Almasan, C. C. Strong Magnetic Fluctuations in a Superconducting State of $CeCoIn_5$. *Phys. Rev. Lett.* **2012**, *108* (5), 056401.
(15) Movshovich, R.; Jaime, M.; Thompson, J. D.; Petrovic, C.; Fisk, Z.; Pagliuso, P. G.; Sarrao, J. L. Unconventional Superconductivity in $CeIrIn_5$ and $CeCoIn_5$: Specific Heat and Thermal Conductivity Studies. *Phys. Rev. Lett.* **2001**, *86* (22), 5152−5155.
(16) Thompson, J. D.; Fisk, Z. Progress in Heavy-Fermion Superconductivity: Ce115 and Related Materials. *J. Phys. Soc. Jpn.* **2012**, *81* (1), 011002.
(17) Kenzelmann, M.; Strässle, Th.; Niedermayer, C.; Sigrist, M.; Padmanabhan, B.; Zolliker, M.; Bianchi, A. D.; Movshovich, R.; Bauer, E. D.; Sarrao, J. L.; Thompson, J. D. Coupled Superconducting and Magnetic Order in $CeCoIn_5$. *Science* **2008**, *321* (5896), 1652−1654.
(18) Gui, X.; Marshall, M.; Dissanayaka Mudiyanselage, R. S.; Klein, R. A.; Chen, Q.; Zhang, Q.; Shelton, W.; Zhou, H.; Brown, C. M.; Cao, H.; Greenblatt, M.; Xie, W. Spin Reorientation in Antiferromagnetic Layered $FePt_5P$. *ACS Appl. Electron. Mater.* **2021**, *3* (8), 3501−3508.
(19) Gui, X.; Xie, W. Crystal Structure, Magnetism, and Electronic Properties of a Rare-Earth-Free Ferromagnet: $MnPt_5As$. *Chem. Mater.* **2020**, *32* (9), 3922−3929.
(20) Gui, X.; Chang, T.-R.; Wei, K.; Daum, M. J.; Graf, D. E.; Baumbach, R. E.; Mourigal, M.; Xie, W. A Novel Magnetic Material by Design: Observation of Yb^{3+} with Spin-1/2 in Yb_xPt_5P. *ACS Cent. Sci.* **2020**, *6* (11), 2023.
(21) Sheldrick, G. M. Crystal Structure Refinement with SHELXL. *Acta Crystallogr., Sect. C: Struct. Chem.* **2015**, *71* (1), 3−8.
(22) Bruker, S. *Bruker SMART*, ver. 5.625; Bruker AXS Inc.: Madison, WI, 2001.
(23) Rodríguez-Carvajal, J. Recent Advances in Magnetic Structure Determination by Neutron Powder Diffraction. *Physica B: Condensed Matter* **1993**, *192* (1), 55−69.
(24) Dinnebier, R. E.; Billinge, S. J. L. *Powder Diffraction: Theory and Practice*; Royal Society of Chemistry, 2008.
(25) Wills, A. S. A New Protocol for the Determination of Magnetic Structures Using Simulated Annealing and Representational Analysis (SARAh). *Physica B: Condensed Matter* **2000**, *276*−*278*, 680−681.
(26) Gui, X.; Klein, R. A.; Brown, C. M.; Xie, W. Chemical Bonding Governs Complex Magnetism in $MnPt_5P$. *Inorg. Chem.* **2021**, *60* (1), 87−96.
(27) Kan, M.; Adhikari, S.; Sun, Q. Ferromagnetism in MnX_2 (X = S, Se) Monolayers. *Phys. Chem. Chem. Phys.* **2014**, *16* (10), 4990−4994.
(28) Kádár, G.; Krén, E. Crystal and Magnetic Structure of the Mn_3Pd_5 Phase. *Solid State Commun.* **1972**, *11* (8), 933−936.
(29) Rashid, M. H.; Sellmyer, D. J. Spin-glass-like Freezing in Disordered $MnPd_3$ and $CrPd_3$ Alloys. *J. Appl. Phys.* **1984**, *55* (6), 1735−1737.
(30) Nieuwenhuys, G. J. Magnetic Behaviour of Cobalt, Iron and Manganese Dissolved in Palladium. *Adv. Phys.* **1975**, *24* (4), 515−591.
(31) Li, M.-R.; Hodges, J. P.; Retuerto, M.; Deng, Z.; Stephens, P. W.; Croft, M. C.; Deng, X.; Kotliar, G.; Sánchez-Benítez, J.; Walker, D.; Greenblatt, M. Mn_2MnReO_6: Synthesis and Magnetic Structure Determination of a New Transition-Metal-Only Double Perovskite Canted Antiferromagnet. *Chem. Mater.* **2016**, *28* (9), 3148−3158.
(32) da Rocha, F. S.; Kakuno, E. M.; Kinast, E. J.; Mazzaro, I.; Fraga, G. L. F. Magnetic and Structural Properties of Pd−Mn−Sn Intermetallics Compounds. *Eur. Phys. J. B* **2011**, *83* (2), 167.
(33) Liu, X.; Taddei, K. M.; Li, S.; Liu, W.; Dhale, N.; Kadado, R.; Berman, D.; Cruz, C. D.; Lv, B. Canted Antiferromagnetism in the Quasi-One-Dimensional Iron Chalcogenide $BaFe_2Se_4$. *Phys. Rev. B* **2020**, *102* (18), 180403.
(34) Lu, W. J.; Sun, Y. P.; Ang, R.; Zhu, X. B.; Song, W. H. Effect of Mo Substitution in the N = 3 Ruddlesden-Popper Compound $Ca_4Mn_3O_{10}$. *Phys. Rev. B* **2007**, *75* (1), 014414.
(35) Speer, S.; Marshall, M.; Chang, H.; Nepal, R.; Blawat, J.; Chapai, R.; Gui, X.; Xie, W.; Jin, R. Mn-Induced Spin Glass Behavior in Metallic $Ir_3Sn_{7-x}Mn_x$. *J. Phys.: Condens. Matter* **2021**, *33* (13), 135701.
(36) Hu, Y.; Chen, C.-W.; Cao, H.; Makhmudov, F.; Grebenkemper, J. H.; Abdusalyamova, M. N.; Morosan, E.; Kauzlarich, S. M. Tuning Magnetism of $[MnSb_4]^{9-}$ Cluster in $Yb_{14}MnSb_{11}$ through Chemical Substitutions on Yb Sites: Appearance and Disappearance of Spin Reorientation. *J. Am. Chem. Soc.* **2016**, *138* (38), 12422−12431.
(37) McGuire, M. A.; Cao, H.; Chakoumakos, B. C.; Sales, B. C. Symmetry-Lowering Lattice Distortion at the Spin Reorientation in MnBi Single Crystals. *Phys. Rev. B* **2014**, *90* (17), 174425.
(38) Zhang, Q.; Tian, W.; Peterson, S. G.; Dennis, K. W.; Vaknin, D. Spin Reorientation and Ce-Mn Coupling in Antiferromagnetic Oxypnictide CeMnAsO. *Phys. Rev. B* **2015**, *91* (6), 064418.
(39) Fabrèges, X.; Petit, S.; Mirebeau, I.; Pailhès, S.; Pinsard, L.; Forget, A.; Fernandez-Diaz, M. T.; Porcher, F. Spin-Lattice Coupling, Frustration, and Magnetic Order in Multiferroic $RMnO_3$. *Phys. Rev. Lett.* **2009**, *103* (6), 067204.
(40) Chan, J. Y.; Olmstead, M. M.; Kauzlarich, S. M.; Webb, D. J. Structure and Ferromagnetism of the Rare-Earth Zintl Compounds: $Yb_{14}MnSb_{11}$ and $Yb_{14}MnBi_{11}$. *Chem. Mater.* **1998**, *10* (11), 3583−3588.
(41) Hirosawa, S.; Matsuura, Y.; Yamamoto, H.; Fujimura, S.; Sagawa, M.; Yamauchi, H. Magnetization and Magnetic Anisotropy of $R_2Fe_{14}B$ Measured on Single Crystals. *J. Appl. Phys.* **1986**, *59* (3), 873−879.
(42) Hirosawa, S.; Sagawa, M. Spin Reorientation and Magnetization Anomaly in $Er_2Fe_{14}B$ and $Tm_2Fe_{14}B$. *Solid State Commun.* **1985**, *54* (4), 335−337.
(43) Kou, X. C.; Grössinger, R.; Hilscher, G.; Kirchmayr, H. R.; Boer, F. R. de. Ac Susceptibility Study on $R_2Fe_{14}B$ Single Crystals (R = Y, Pr, Nd, Sm, Gd, Tb, Dy, Ho, Er, Tm). *Phys. Rev. B* **1996**, *54* (9), 6421−6429.
(44) Qi, B.; Perez, I.; Ansari, P.; Lu, F.; Croft, M. Croft, M. L_2 and L_3 Measurements of Transition-Metal 5*d* Orbital Occupancy, Spin-Orbit Effects, and Chemical Bonding. *Phys. Rev. B* **1987**, *36* (5), 2972.
(45) Perez, I.; Qi, B.; Liang, G.; Lu, F.; Croft, M.; Wieliczka, D. Spectroscopic Results on the above and below E_F Electronic Structure of TAl_2, T= Au and Pt. *Phys. Rev. B* **1988**, *38* (17), 12233.
(46) Chen, J.; Croft, M.; Jeon, Y.; Xu, X.; Shaheen, S.; Lu, F. X-Ray-Absorption-Spectroscopy Studies of Transition-Metal−Boron Compounds. *Phys. Rev. B* **1992**, *46* (24), 15639.
(47) Jeon, Y.; Chen, J.; Croft, M. X-Ray-Absorption Studies of the d-Orbital Occupancies of Selected 4d/5d Transition Metals Compounded with Group-III/IV Ligands. *Phys. Rev. B* **1994**, *50* (10), 6555.
(48) Chae, K.; Jung, S.; Lee, Y.; Whang, C.; Jeon, Y.; Croft, M.; Sills, D.; Ansari, P.; Mack, K. Local Density of Unoccupied States in Ion-Beam-Mixed Pd-Ag Alloys. *Phys. Rev. B* **1996**, *53* (15), 10328.
(49) Lee, Y.; Whang, C.; Jeon, Y.; Choi, B.; Han, T.; Woo, J.; Croft, M. Study of the L3 Edges of Ion-Beam-Mixed Pd-Cu Alloys by X-Ray Absorption Spectroscopy. *Nucl. Instrum. Methods Phys. Res., Sect. B* **1997**, *129* (3), 387−391.
(50) Ruckman, M.; Reisfeld, G.; Jisrawi, N. M.; Weinert, M.; Strongin, M.; Wiesmann, H.; Croft, M.; Sahiner, A.; Sills, D.; Ansari, P. XANES Study of Hydrogen Incorporation in a Pd-Capped Nb Thin Film. *Phys. Rev. B* **1998**, *57* (7), 3881.

https://doi.org/10.1021/acs.inorgchem.1c03637
Inorg. Chem. 2022, 61, 3981−3988